photonics

MDPI

Article

Research on the Dynamic Evolution of Optical Fiber Excess Length and Icing Monitoring for In-Service Power Optical Cables in Extremely Cold Environments

Yihong Li [1], Liwen Hu [1,*] and Chunsheng Li [2]

[1] School of Physics and Electronic Science, Changsha University of Science and Technology, Changsha 410076, China
[2] Institute of Huafei, Beijing University of Posts and Telecommunications, Beijing 100876, China
* Correspondence: lwhu214@csust.edu.cn

Abstract

In extremely cold regions, OPGW optical cables are prone to anomalies due to icing, especially when their internal fiber length is easily depleted, which then seriously affects the normal operation of the entire power communication system. Therefore, this paper proposes a nonlinear inversion analysis method that couples catenary theory with biaxial statics to monitor the variation of the FEL under extreme icing conditions. First, the quantitative mapping relationship between BFS and the dynamic evolution of FEL has been established, and a three-dimensional response model, encompassing tension, ice thickness, and FEL has been constructed. Subsequently, an inversion algorithm for ice thickness based on BOTDR frequency shift signals has been developed by introducing horizontal tension as a key intermediate physical quantity. When the FEL decreases from 0.2% to 0.1%, the corresponding EIT can evolve from 0.08 m to 0.16 m approximately, indicating that the system has entered a warning zone characterized by a sharp increase in strain. The proposed model has successfully achieved the transition of distributed monitoring theory from physical perception to quantitative inversion, thereby providing theoretical support for early ice warning and disaster prevention assessments of in-service power optical cables.

Keywords: Brillouin Optical Time Domain Reflectometry; catenary; fiber excess length; ice warning; fiber strain; brillouin frequency shift; equivalent ice thickness

1. Introduction

After nearly 60 years of development, the manufacturing process of optical fiber cables has become highly mature [1]. The redundant portion by which the actual physical length of optical fiber inside optical cable exceeds the reference length of its structure is referred to as the fiber excess length (FEL), which is typically quantified by the excess length ratio, generally ranging from 0.1% to 0.7% [2]. Its core function is to provide strain buffering for optical cables and is also the critical mechanical criterion in the design of optical cable structures [3]. With the continuous improvement in the design of fiber excess length for power optical cables, the usage of them has been increasing year by year [4,5]. Between the first limited adoption in 2000 and the present large-scale deployment, the Optical Fiber Composite Overhead Ground Wire (OPGW) has become one of the most widely used types of specialized power optical cables in power communication systems [5,6]. However, under extreme adverse climatic conditions such as strong winds, low temperatures, severe cold,

Check for updates

Received: 23 August 2026
Revised: 23 September 2026
Accepted: 29 September 2026
Published: 5 October 2026

Copyright: © 2026 by the authors. Licensee MDPI, Basel, Switzerland. This article is an open access article distributed under the terms and conditions of the Creative Commons Attribution (CC BY) license.

or icing, OPGW cables do experience elongation or contraction during operation due to the effects of mechanical stress or temperature variations, along with corresponding changes in their sag, which consequently lead to corresponding variations in the fiber excess length of power optical cables [7,8]. These can exert a significant impact on the entire in-service power optical cable link. For instance, the fiber excess length increases when an optical cable contracts due to low-temperature conditions. Then, the optical fiber can undergo macro-bending within the optical unit, leading to increased additional attenuation across the entire link and communication abnormalities, which ultimately poses considerable challenges to the power system [8,9]. Notably, the pre-configured redundant fiber excess length is preferentially consumed by the tightening of slack sections or straightening of helical structures when OPGW undergoes axial stretching induced by ice loading or thermal expansion and contraction, which allows the optical fiber to remain in a safe state without directly bearing tensile stress within a certain threshold, thereby ensuring the stability of optical signal transmission [10]. However, once the cable elongation caused by external loads exceeds the initial excess fiber length, the optical fiber will rapidly enter a stress-sensitive region and induce increased micro-bending loss or even fracture, thereby seriously jeopardizing the communication security of the power system [11,12]. Clearly, early monitoring and prevention of this phenomenon hold significant theoretical guidance and practical engineering value for the subsequent maintenance of power optical cables.

Currently, Distributed Fiber Optic Sensing (DFOS) technology, by virtue of its unique advantages such as long sensing distance, real-time capability, and immunity to electromagnetic interference, has become a mainstream approach for monitoring ice accretion and strain on in-service optical cables [13,14]. Meaningfully, Brillouin Optical Time Domain Reflectometry (BOTDR) has been the most widely adopted technique [13–17]. Nevertheless, the existing monitoring models still face obvious theoretical bottlenecks when inverting ice thickness or stress states. For instance, the conventional inversion models are often predicated on the assumption of deformation synchronicity and fail to adequately account for the strain shielding effect induced by FEL and its resulting temporal lag in the response of Brillouin frequency shift (BFS) signals [15,18]. In engineering practice, these issues can result in a sensing blind zone during the early stage of icing, when the FEL has not yet been exhausted. In the subsequent inversion calculations, after the FEL has been fully consumed, the lack of a precise determination of the initial FEL leads to significant deviations in the inverted ice thickness data. However, the traditional cutback method employed as a remedial measure is destructive, and the high-precision Optical Frequency Domain Reflectometry (OFDR) is constrained by its limited measurement distance [18]. Apparently, neither approach can meet the requirements to enable dynamic assessments of long-span, long-distance in-service cable lines.

Therefore, this paper proposes a monitoring model for the FEL and ice accretion of in-service power optical fiber cables which integrates macroscopic geometric mechanics with microscopic strain transfer analysis. First, the catenary theory is employed to construct a macroscopic topological deformation model of the OPGW under ice loading. Subsequently, static mechanical analysis is applied to elucidate the mechanical coupling mechanism between cable tension variation and internal fiber excess length consumption, thereby establishing a quantitative mapping relationship between the onset inflection point of BFS response and the initial FEL. Then, an inversion algorithm for ice thickness based on BOTDR-BFS is established by introducing horizontal tension as a key intermediate physical quantity. Experimental results under different operating conditions are basically in good agreement with theoretical simulations. The proposed model can effectively break through the interference bottleneck that the FEL factor has an impact on the accuracy of distributed

sensing, which thereby provides theoretical support for early warning of ice damage and refined operation and maintenance in power communication links.

2. Materials and Methods

2.1. Fiber Excess Length (FEL)

From a macroscopic geometric perspective, the FEL is not simply a length redundancy, but a strain buffering mechanism constructed by a nonlinear arrangement of fibers within the optical cable, such as spiral twisting or sine wave shape [2,10], as shown in Figure 1. The lower part of the figure shows the entire optical cable containing optical fiber, while the upper part illustrates the optical fiber portion inside the cable. When the optical cable is subjected to external axial tension, the optical fiber absorbs the deformation through contraction of the helical radius or flattening of the wavy configuration, thereby delaying the time of strain experienced by the fiber itself. The subsequent parts of this paper utilize this concept to preferentially absorb the elongation of the cable body through the rewinding of the fiber geometry under external loads such as icing, thereby retarding the axial force on the fiber itself and ultimately ensuring the stable transmission of optical signals under external load fluctuations. Obviously, the FEL is continuously consumed during this process [8]. Specifically, the consumption of the FEL is not a reduction in the length of the optical fiber, but a process in which the optical fiber transforms from a spatially bent shape to an axially stressed state. Its mathematical meaning is a threshold effect of strain transmission, which means that only when the elongation of the optical cable exceeds the threshold set by the initial excess length is the strain transmitted to the inside of the optical fiber [10,19].

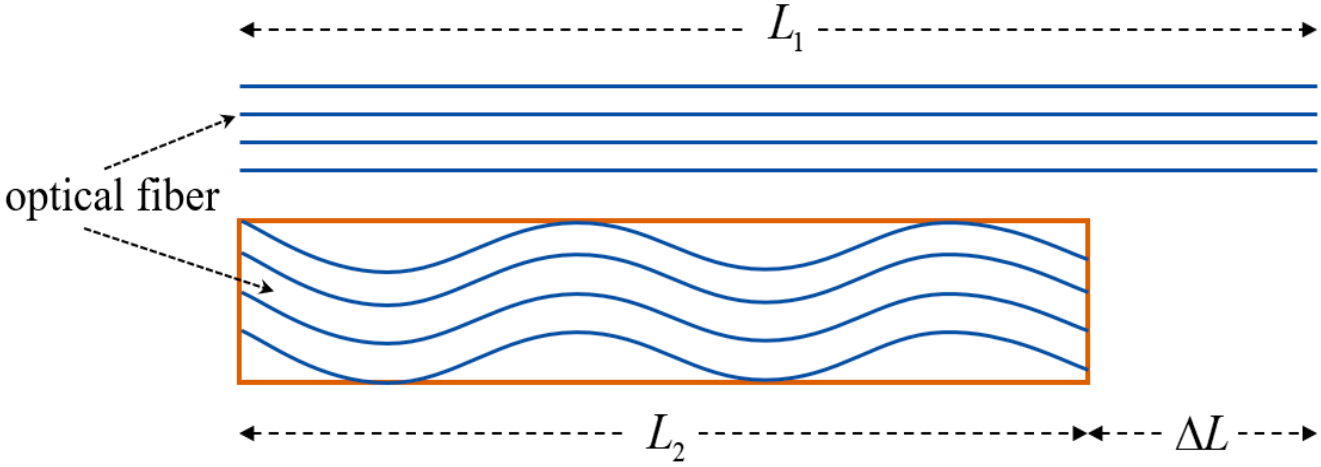

Figure 1. Schematic diagram of the FEL principle.

Let the structural reference length of an optical cable segment be L_2, and the actual physical length of the optical fiber encapsulated therein be L_1. The reserved FEL is denoted as η, which can be calculated using Equation (1) [2].

$$\eta = \frac{L_1 - L_2}{L_2} \times 100\% \quad (1)$$

According to the initial spatial distribution of the optical fiber within the loose tube and its characteristic changes before and after deformation as illustrated in Figure 1, it can be understood that by clarifying the proportional relationship between the actual fiber length L_1 and the reference cable length L_2, the process of excess fiber length consumption, namely the physical process in which L_2 dynamically approaches L_1, can be revealed. Its key

significance lies in revealing the geometric compensation function exhibited by the wavy configuration of the optical fiber. For instance, this special configuration can convert the macroscopic axial displacement of the optical cable into the spatial geometric unwinding of the internal optical fiber during the initial stage of loading, thereby establishing an effective geometric shielding interval that ensures the optical fiber does not experience direct axial stress until the FEL is fully consumed. This also lays a theoretical foundation for subsequent nonlinear inversion studies that utilize distributed sensing technology to investigate the transition of optical fibers in cables from geometric displacement to axial strain. The elongation of the optical cable can gradually approach the initial surplus length of the optical fiber as the external load continues to increase, at which point the optical fiber begins to transition from a relaxed state to a stressed state. Notably, this critical point corresponds to the moment when the FEL is completely exhausted, which is also the dynamic inflection point where the BFS transitions from a stable plateau to a linear growth [18,20]. Therefore, accurately identifying this turning point serves as a fundamental prerequisite for the subsequent inversion of the FEL consumption state using BOTDR signals.

2.2. Fiber Strain and BFS Under Ice Loading

As is well known, the optical signals can interact with the fiber optic medium and produce scattered light during the transmission process of optical cables and fibers [5,13]. In the context of optical signal transmission through optical cables, there are three main types of scattered light, namely Rayleigh scattering, Brillouin scattering and Raman scattering [20]. Among them, Brillouin scattering is a special scattering phenomenon caused by inelastic collisions between photons and phonons within an optical fiber medium [13]. The energy exchange occurs between photons and phonons during the collision process, whereby a photon may either transfer a portion of its energy to a phonon or acquire energy from a phonon. Such energy transfer directly leads to a change in the frequency of the incident light wave [15,18]. According to the existing classical literature [13–18], the frequency of the scattered light wave forms a fixed difference with that of the incident light wave, which is defined as BFS and represented by Equation (2).

$$v_B = \frac{2nV_a}{\lambda} \tag{2}$$

where n is the refractive index of the optical fiber, λ is the incident light wavelength, and V_a is the optical fiber average sound velocity expressed in meters per second, which can be calculated using Equation (3) [2,21].

$$V_a = \sqrt{\frac{(1-k)E}{(1-2k)(1+k)\rho}} \tag{3}$$

where k is the Poisson's ratio of the optical fiber, E is the elastic modulus of the optical fiber in Pa, and ρ is the density of the optical fiber in kg/m3.

When the ambient temperature T surrounding the optical fiber fluctuates or the strain ε it experiences changes, the core physical parameters such as the refractive index, Poisson's ratio, Young's modulus, and optical fiber density all undergo varying degrees of alteration under the combined influence of the thermo-optic effect and elasto-optic effect of the optical fiber [11,20]. The instantaneous value of v_B during such variations can be obtained by combining Equations (2) and (3) as then expressed by Equation (4).

$$v_B = \frac{2n(T,\varepsilon)}{\lambda} \times \sqrt{\frac{1-k(T,\varepsilon)E(T,\varepsilon)}{[1-2k(T,\varepsilon)][1+k(T,\varepsilon)]\rho(T,\varepsilon)}} \tag{4}$$

A careful analysis of Equation (4) reveals that the BFS ν_B is a nonlinear function of the refractive index n, Poisson's ratio k, Young's modulus E, and fiber density ρ. Its theoretical calculation involves considerable complexity. Notably, these parameters all exhibit significant sensitivity to both temperature and strain [22]. In practical engineering applications, a first-order Taylor expansion is commonly applied to Equation (4) to simplify the analysis and extract the core physical quantities. Through subsequent derivation, the linear relationship between the BFS variation $\Delta\nu_B$ and the temperature variation ΔT as well as the strain variation $\Delta\varepsilon$ can be obtained and expressed by Equation (5) [23,24].

$$\Delta v_B = C_\varepsilon \Delta\varepsilon + C_T \Delta T \tag{5}$$

where C_ε and C_T denote the strain coefficient and temperature coefficient, respectively. For a standard single-mode optical fiber, C_ε is taken as 0.05 MHz/με and C_T as 1.07 MHz/°C.

It is worth noting that the sensitivity of the BFS to temperature is significantly lower than its sensitivity to strain [22–24]. Given the research focus of this study, the mechanical response of optical cable fiber induced by ice loading is analyzed as the primary concern. Accordingly, the ambient temperature of the optical cable has been maintained under constant conditions in the subsequent experiments and simulations conducted herein. In the ice monitoring scenario considered in this study, the BFS variation ($C_T\Delta T$) induced by temperature fluctuations is far smaller than that ($C_\varepsilon\Delta\varepsilon$) caused by strain variations resulting from ice loading. Taking a typical operating condition as an example, ΔT usually does not exceed ±5 °C, whereas $\Delta\varepsilon$ can reach several thousand microstrains. Thus, the contribution of the former to the total frequency shift is typically less than 10% [18]. This study temporarily disregards the coupling interference induced by temperature fluctuations in analyzing the mechanical evolution dominated by ice loading and sets $\Delta T = 0$. Then, Equation (5) can be simplified to a linear mapping relation driven solely by strain, as expressed by Equation (6).

$$\Delta v_B = C_\varepsilon \Delta\varepsilon \tag{6}$$

Here, it serves as a fundamental model for strain inversion. References [13–15] demonstrate that BOTDR acquires strain information along the optical cable fiber by monitoring the state value of the BFS ν_B. Thus, the BFS variation $\Delta\nu_B$ measured by BOTDR can directly reflect the axial strain $\Delta\varepsilon$ of the optical fiber when it is in a stressed state, while the corresponding $\Delta\nu_B$ exhibits no significant change when the optical fiber is in a relaxed state, namely $\Delta\varepsilon = 0$. In addition, BOTDR distributed measurement follows the temporal logic of that positioning first, frequency measurement later. That is, the time required for the backward Brillouin scattering light generated at different positions to return to the receiving end is different after the probe light pulse is injected into the optical fiber, and consequently the system continuously records the scattering signals at each time instant [13,20]. Then, based on the time delay of sending the probe light and receiving the scattered light, the positioning function can be applied and the distance calculation formula between a certain point of the optical fiber and the incident end can be expressed via Equation (7).

$$h = \frac{c\Delta t}{2n} \tag{7}$$

where c is the speed of light in m/s and Δt represents the time difference between sending the probe light and receiving the scattered light. Then, each return time Δt is converted into the corresponding optical fiber distance L by using Equation (7), thereby determining the specific location on the optical fiber from which the scattering signal originates. Subsequently, spectral analysis is performed on the time window corresponding to that position

to extract the BFS peak value $\Delta\nu_B(L)$. Consequently, the complete distance–frequency shift distribution curve can be obtained.

2.3. FEL Evolution Modeling

As discussed above, the strain shielding effect constructed by the FEL is the root cause of the hysteresis observed in BOTDR sensing signals in the icing monitoring system for overhead power optical cables [7,25]. The length margin reserved for optical fiber within the loose tube essentially constitutes a process of forming a mechanical buffer barrier from the perspective of the microscopic mechanism of strain transfer [16]. During this period, provided that macroscopic elongation of the optical cable has not yet exceeded the geometric threshold set by the initial FEL, the optical fiber can absorb the cable body deformation through adaptive reconfiguration of its topological configuration, such as contraction of the helical radius or flattening of the wavy pattern, during which the axial stress perceived by the fiber itself is negligible [18]. Then, upon introducing the equivalent FEL occupancy rate $\tau = \varepsilon_c / \eta_0$, this shielding interval can be concisely expressed as $\tau \leq 1$, where ε_c denotes the cable strain and η_0 represents the initial FEL. Within this interval, the fiber strain ε measured by BOTDR remains consistently zero and the BFS signal presents a stable low-sensitivity plateau period, thus placing the monitoring system in a sensing blind zone with respect to the ice loading.

To overcome the aforementioned limitation, this study transforms the sensing blind zone originally regarded as a monitoring obstacle into a critical dynamic window for characterizing the state of FEL consumption. At the macroscopic level, the catenary equation [26] is employed to precisely describe the continuous evolution of the suspension form of optical cables driven by icing loads and solve for the arc length path integral that varies with ice thickness. Then, the macroscopic geometric deformation is transferred to the microscopic static analysis of the optical fiber [2,27] so as to analyze strain transfer efficiency of the helical stranding structure under tension. Further, a coupled catenary-static biaxial tension inversion model is established. Through this dual-layer coupling framework, a nonlinear mapping from the macroscopic catenary slope to the microscopic axial strain of optical fiber is realized, thereby establishing a quantitative relationship between cable elongation and FEL consumption from a mechanical perspective. For the suspended optical cable, each BFS measured by BOTDR can be inverted with the help of the catenary-static coupling model to determine the initial FEL required to maintain zero fiber strain under that specific operating condition, at which point the equivalent FEL occupancy rate is $\tau = 1$. The BFS value itself serves as a form of the dynamic encoding of the current icing condition. Specifically, $\tau = 0$ represents the initial design baseline, while $\tau = 1$ denotes the critical trigger point, beyond which the system enters linear strain response regime. Therefore, each set of frequency shift data corresponds to an initial FEL value that is dynamically updated with the operating condition, thus realizing an essential transformation of the FEL from a static constant at the factory to a dynamic parameter in service. Meaningfully, this paradigm shift from physical masking to feature-driven characterization not only corrects the initial data distortion caused by FEL shielding to ensure that the equivalent ice thickness obtained through inversion within the critical stress range, where the FEL is consumed to 0.1~0.2%, can faithfully reflect the true condition of the line, but also achieves a digital characterization of the entire process for in-service optical cables, spanning from geometric relaxation to the critical stress threshold.

Under the framework of the equivalent FEL occupancy rate, the relationship among the fiber strain ε, the cable strain ε_c and the initial FEL η_0 can be uniformly expressed as a piecewise function with respect to the equivalent FEL occupancy rate τ. When $\tau \leq 1$, the cable elongation has not yet reached the geometric threshold set by the initial FEL and the

optical fiber remains in a completely relaxed state. Once $\tau > 1$, the initial FEL has been fully consumed, and the optical fiber begins to bear axial strain together with the cable, with its strain magnitude equal to the portion of cable elongation exceeding the initial FEL. This evolutionary behavior can be expressed by Equation (8).

$$\varepsilon = \begin{cases} 0, & \tau \leq 1 \\ \varepsilon_c - \eta_0, & \tau > 1 \end{cases} \tag{8}$$

To highlight the focus of this paper and eliminate unnecessary interference, it is assumed that optical fiber is in the form of an equal height catenary, as shown in Figure 2a.

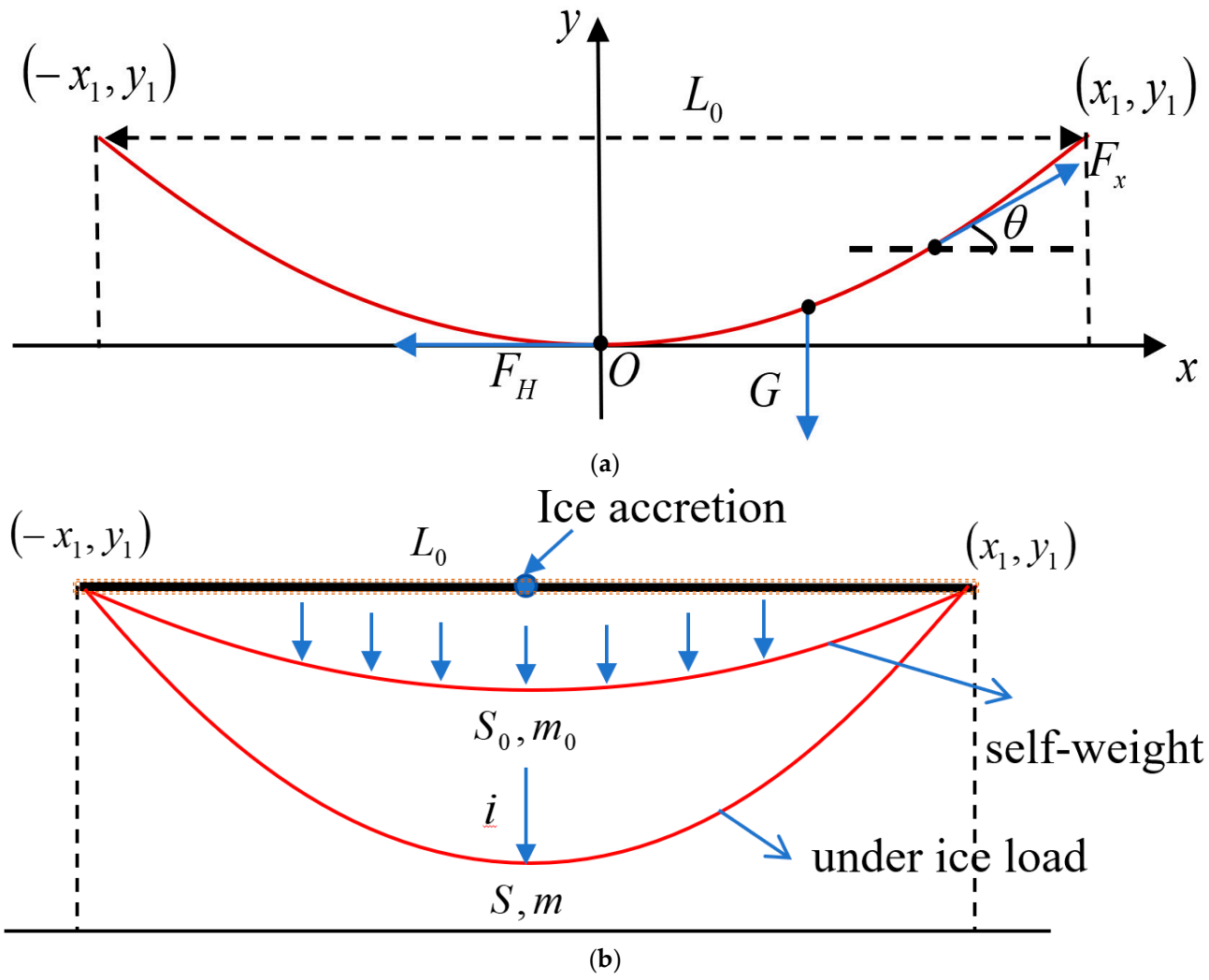

Figure 2. Schematic diagram of the theoretical structure of optical fiber suspension (**a**). Fiber optic force analysis; (**b**). Evolution of the catenary under self-weight and ice load.

In Figure 2a, L_0 denotes the horizontal span between the two suspension points, $(-x_1,y_1)$ and (x_1,y_1) are the coordinates of the left and right suspension points, respectively, O is the lowest point of the catenary, F_H is the horizontal tension at the lowest point, F_x is the axial tension at an arbitrary point on the fiber, θ is the inclination angle between the tangent at the arbitrary point and the horizontal direction, and G is the gravitational force of the fiber segment from the lowest point O to the arbitrary point. Notably, these parameters satisfy the static equilibrium condition in Equation (11) (mentioned later) and thus are used in the catenary equation, Equation (12), the arc length formula, Equation (13), and the coupling model, Equations (14)–(20). In Figure 2b, the OPGW forms an initial

catenary with arc length S_0 and total mass m_0 under the self-weight only, as indicated by the upper curve and the downward arrows labeled "self-weight". The additional ice load increases the total mass per unit length when ice accretes on the cable surface, causing the catenary to sag further to a new equilibrium, as indicated by the lower curve with arc length S and total mass m and the downward arrows labeled "under ice load". The equivalent ice thickness on the cable surface is denoted by i. As i increases, the total load increases, and thus the sag and arc length increases from S_0 to S. Therefore, the FEL is gradually consumed. Moreover, the fiber remains stress-free and the BFS stays at a stable plateau before the FEL is exhausted ($\tau \leq 1$). It begins to bear axial strain, and the BFS shifts linearly with the applied ice load, once $\tau > 1$. Then, a quantitative correlation between the BFS variation and the optical fiber strain can be further established by analyzing the tension distribution along the line, the evolution law of which can be expressed by Equation (9).

$$\Delta v_B = \begin{cases} 0, & \tau \leq 1 \\ C_\varepsilon \cdot (\varepsilon - \varepsilon_0), & \tau > 1 \end{cases} \tag{9}$$

where ε_0 denotes the initial strain of the optical fiber. Notably, within the elastic range of the optical fiber, stress and strain satisfy $\sigma = E\varepsilon$, while the tension and stress at any arbitrary point satisfy $F = \sigma A$. The tension can be transformed into an equation incorporating the BFS [21,23] as expressed by Equation (10).

$$F_x = \frac{AE(\Delta v_B + C_\varepsilon \varepsilon_0)}{C_\varepsilon} \tag{10}$$

where A represents the cross-sectional area of the optical fiber. Equation (10) reveals the relationship between the tension at any point on the optical fiber and the BFS and enables the analytical conversion from microscopic frequency shift characteristics to macroscopic tension information. Returning to Figure 2, a careful analysis reveals that the catenary structure of the optical fiber satisfies the conditions of static equilibrium [26,27], whose equilibrium equation is expressed as shown in Equation (11).

$$F_x{}^2 = G^2 + F_H{}^2 \tag{11}$$

From a macro perspective, the suspension trajectory of the optical fiber between two equally high support points satisfies the catenary equation [25,27] and can be represented by Equation (12).

$$y = \frac{F_H}{q_f} \cosh\left(\frac{x q_f}{F_H}\right) - \frac{F_H}{q_f} \tag{12}$$

where q_f denotes the mass per unit length of optical fiber. The arc length formula can be derived and then expressed in Equation (13) by analyzing the trajectory equation.

$$S = \int_0^x \left(1 + \left(\frac{\partial y}{\partial x}\right)^2\right)^{1/2} dx = \frac{F_H}{q_f} \sinh \frac{q_f x}{F_H} \tag{13}$$

Equation (13) establishes an intrinsic link between the geometric configuration of optical cable and the mechanical response of optical fiber, with its core lying in accurate quantification of the gravitational loading. Although conventional monitoring methods such as the weighing method can obtain macroscopic gravitational information, they tend to treat the macroscopic catenary trajectory and the internal strain transfer law in isolation, consequently struggling to balance real-time monitoring capability with data accuracy [8,22]. While the catenary equation can describe the overall morphology of optical cable, it suffers from limitations in the accuracy of the parameter extraction [26].

Although the strain analysis based on the static equilibrium conditions can precisely capture local details, it struggles to reflect the macroscopic topology of cable line [27]. Therefore, the ratio of gravitational force to horizontal tension at the lowest point is introduced as a characteristic variable, denoted as K, by coupling the advantages of the two aforementioned models. Then, a monitoring model that combines global enveloping and local accuracy is constructed and represented by Equation (14) by analyzing the nonlinear relationship between the slope of the catenary and the length of the optical cable.

$$G = q_f S = F_H \sin \mathrm{h} \frac{Gx}{F_H S} \tag{14}$$

Furthermore, the arc length and the force can be completely decoupled by performing a transformation on Equation (14), thus enabling the FEL to be correlated with the BFS, which also can be described by Equation (15).

$$K = \tan \theta = \frac{G}{F_H} = \sin \mathrm{h} \frac{Gx}{F_H S} \tag{15}$$

Then, by substituting Equation (15) into Equation (14) and performing a mathematical transformation, the relationship between the arc length and the catenary slope can be acquired and expressed by Equation (16).

$$S = \frac{Kx}{\ln[K + (1 + K^2)^{1/2}]} \tag{16}$$

Subsequently, a quantitative calculation formula for the evolution of arc length with BFS can be derived by adding Equation (10), which can be represented by Equation (17).

$$S = \frac{x\sqrt{a^2 - b^2}}{b \ln\left(\frac{\sqrt{a^2 - b^2} + a}{b}\right)} \tag{17}$$

where $a = F_x = AE(\Delta\nu_{BX} + C\ _{\varepsilon}\varepsilon_{0X})/C_{\varepsilon}$, $b = F_H = AE(\Delta\nu_{BH} + C_{\varepsilon}\ \varepsilon_{0H})/C_{\varepsilon}$, $\Delta\nu_{BX}$ is the BFS at any arbitrary point of optical fiber, and $\Delta\nu_{BH}$ is the BFS at the lowest point. Further, by integrating over the spatial path, Equation (16) establishes a topological mapping between the macroscopic geometry of the cable and the microscopic mechanical response of the fiber and achieves the transformation of the FEL from the design constant to the dynamic characteristic parameter. This not only elucidates, from a mechanical perspective, the influence of the strain shielding effect on the BFS, but also provides a crucial logical closure for next establishing the mapping relationship between the FEL and ice thickness through the introduction of geometric constraints. For ease of subsequent analysis, it is still simplified to Equation (18).

$$S = \frac{xc}{z} \tag{18}$$

where $c = \sqrt{a^2 - b^2}$ and $z = bln\left[\left(\sqrt{a^2 - b^2} + a\right)/b\right]$. Then, an exact expression for the FEL can be obtained by combining Equation (1), and represented by Equation (19).

$$\eta = \frac{2S}{L_0} - 1 \tag{19}$$

where L_0 denotes the distance between the two endpoints. Since the arc length S solved by Equation (16) denotes the unilateral arc length from the lowest point O of the catenary to an arbitrary point x of optical fiber, whereas the FEL $\eta = (2S - L_0)/L_0$ solved in Equation (19) requires consideration of the total arc length of entire suspending fiber segment, it is necessary to take $2S$ when substituting Equation (18) into Equation (19) in order

to cover the bilateral symmetric arc length from the suspension points to the lowest point. Furthermore, by setting $x = L_0/2$, i.e., taking the arbitrary point x at the right suspension point, the exact expression for the FEL of the whole suspended fiber segment can be obtained after rearrangement and expressed by Equation (20).

$$\eta = \frac{c}{z} - 1 \tag{20}$$

Thus, a quantitative mapping relationship between the tension characterized by the BFS and the FEL is established, which enables a direct inversion from BOTDR-measured frequency shift values to the FEL in the current operating. In brief, Equation (20) transforms the FEL from a static design value fixed at the time of manufacture, which merely reflects the initial structural state of the optical cable, into a dynamic characteristic parameter that is updated in real time with the ice loading condition. Using Equation (20), each set of frequency shift data can be used to calculate a corresponding FEL value, which can quantitatively characterize the reserved length margin, namely the buffer arc length required for the optical fiber within the loose tube, that is necessary to counteract the macroscopic deformation of the optical cable and ensure that the fiber remains free of axial stress under the current icing conditions. This transformation elevates the FEL from a mere number on a design drawing to a physical quantity that can be monitored in real time and tracked dynamically. Serving as a key input parameter, it directly underpins the subsequent investigation about the ice thickness inversion algorithm and is also the central bridge connecting the preceding and following stages of analysis chain from frequency shift measurement to FEL inversion and then to ice thickness output.

2.4. Equivalent Ice Thickness Inversion Modeling

Through the construction of a coupled catenary-static bilayer model, this paper has systematically elucidated the dynamic evolution mechanism of the FEL under complex cable loads, explored the mechanical mapping between macroscopic topological deformation and microscopic configurational reconstruction, and laid a profound causal foundation for the subsequent demodulation of the sensing signals. Only by precisely deconstructing the dynamic pathway through which the FEL evolves from geometric shielding to stress triggering can the monitoring bottleneck induced by response hysteresis be overcome. Further, building upon this rigorous mechanical constraint, the strain transfer characteristics driven by ice loading will be made the target of further investigations. It translates the dynamic FEL characteristic parameter obtained previously into a core criterion for an inversion model, thus constructing a high-fidelity inversion algorithm for equivalent ice thickness based on BOTDR-BFS. Clearly, this logical progression from mechanism analysis to algorithm reconstruction not only ensures the coherence and completeness of the research framework presented, but also provides a closed-loop theoretical and technical foundation for eliminating the initial sensing blind zone and improving the monitoring accuracy of long-span in-service optical cable lines.

The actual ice accretion morphology on the surface of OPGW exhibits obvious diversity and irregularity [23]. To establish a standardized evaluation system for ice thickness and ensure the universality of its calculation results, many researchers typically simplify the complex ice cross-section into an equivalent cylindrical model for mechanical derivation [14,25]. To focus the research, it is assumed here that the ice accretion on the optical cable is uniformly distributed and that no transverse wind load is present. At this time, the total gravity load per unit length of optical cable is only composed of the self-weight of the optical cable, including the weight of the

cable shell and the weight of the internal optical fiber, and the vertical component of the ice weight. Subsequently, the Equivalent Ice Thickness (EIT) is introduced to characterize this condition, which can be expressed by Equation (21). Its specific value can be obtained through inversion based on the measured ice mass [28,29].

$$m_i = m - m_0 = \rho_i \pi S \left[\left(i + \frac{d}{2} \right)^2 - \frac{d^2}{4} \right] \tag{21}$$

where i denotes the cable surface EIT, obtaining by simplifying the actual ice accretion on the outer cable sheath into an equivalent cylindrical model. It represents the macroscopic meteorological ice load on the OPGW and is used for design-oriented safety margin assessments. Here, the measured data of the bare fiber are used to obtain the arc length more accurately, which then can be used to invert the icing load on the bare optical fiber as well as the icing load on the cable, thereby providing a unified geometric basis for cross-scale inversion of icing loads from the fiber level to the cable level. In these calculations, m_i is the ice mass; m is the total weight; m_0 is the net mass of optical cable; ρ_i is the ice density; and d is the cable diameter. Further, the two precise calculation formulas are provided by Equations (22) and (23).

$$i = \sqrt{\frac{m - m_0}{\rho_i \pi S} + \frac{d^2}{4}} - \frac{d}{2} \tag{22}$$

and

$$m = \frac{F_c \sin\theta}{g} \tag{23}$$

where F_c is the tension of optical cable, the value of which corresponds to the tension at the moment when the cable strain exactly reaches the FEL, i.e., $\varepsilon_c = \eta_0$. At this critical state, the optical fiber is free from stress, with its stress being negligible compared to that of the cable. Thus, only a small strain in optical fiber is required to obtain the BFS, from which the accurate arc length and the sine and cosine values of the cable can be subsequently derived. Therefore, the calculation of cable tension only needs to consider the strain at this critical state, which also obeys Hooke's law [30,31], namely $F_c = \sigma_c A_c$, where σ_c is the stress experienced by the optical cable and A_c is its cross-sectional area. Furthermore, since $\sigma_c = E_c \varepsilon_c$ and $\varepsilon_c = \eta_0$, where E_c is the Young's modulus of the optical cable, and noting that $sin\theta$ is the sine value of the cable at position x, which can be displayed in terms of F_x and F_H, the exact expression for the total mass can be obtained and then represented by Equation (24).

$$m = \frac{F_c \sin\theta}{g} = \frac{A_c E_c \eta_0 \sqrt{a^2 - b^2}}{ag} \tag{24}$$

Returning to Figure 2, the bare fiber is suspended on two fixed pulleys, and as the applied load increases, the fiber will provide additional length through internal compensation. It is now assumed that the segment of optical fiber between the two endpoints is equipped with a cable sheath whose mass does not change with the increase in the internal fiber length. Notably, its variations merely result in synchronous elongation of the sheath without causing any change in its mass. So here, only the geometric compensation of the optical fiber inside the cable is considered, without accounting for the axial compensation of the sheath itself. Moreover, since the gravity per unit length of the internal optical fiber differs from that of the overall cable structure by several orders of magnitude, the extremely weak gravity component contributed by the compensating fiber segment can be neglected in practical engineering modeling. Then, the uniform gravity per unit length of the entire cable is simplified to q_0. Consequently, the total mass of the optical cable depends

only on the measurement point x along the cable line direction and can be calculated by Equation (25).

$$m_0 = \frac{q_0 x}{g} \tag{25}$$

By combining Equations (22) through (25) and substituting the BFS parameters into them, the exact expression for the EIT can be obtained and expressed by Equation (26).

$$i = \sqrt{\frac{z[A_c E_c \eta_0 c - q_0 a x]}{u_0 x a c} + \frac{d^2}{4}} - \frac{d}{2} \tag{26}$$

where $u_0 = \pi \rho_i g$. Heavier ice accretion necessitates a larger initial FEL to provide a direct theoretical basis for differentiated structural designs of optical cables. In engineering practice, the initial FEL design parameter η_0 can be set equal to η, meaning that η_0 is expressed as a direct function of the ice thickness i, i.e., $\eta_0 = \eta(i)$. This transformation upgrades the design logic of the FEL from a uniform configuration to a customized design tailored to ice thickness. Consequently, designers can directly read the required minimum FEL setting from this equation based on the target ice grade for the region where the line is located, thereby striking an optimal balance between tensile failure due to insufficient FEL and bending fatigue due to excessive FEL. Thus, for optical fiber suspended at equal heights, i.e., $x = L_0/2$, the exact expression for the FEL can be obtained by combining Equation (18b) with Equation (26), which then is expressed by Equation (27).

$$\eta_0 = \eta(i, \beta) = \frac{1}{A_c E_c \sqrt{1-\beta^2}} \left[\frac{q_0 L_0}{2} + \frac{u_0 L_0 \sqrt{1-\beta^2}(i^2 + id)}{2\beta ln\left(\frac{1+\sqrt{1-\beta^2}}{\beta}\right)} \right] \tag{27}$$

where $\beta = cos\theta = b/a$. Apparently, there exist substantial differences in required initial FEL (η_0) under different ice thickness conditions, namely, the heavier the ice accretion, the greater the required initial FEL, which provides a direct mathematical basis for differentiated structural design. Furthermore, Equations (26) and (27) reconstruct the FEL from the static constant into a dynamic adjustment operator that varies with operating conditions, collectively constituting the mathematical core of the ice monitoring algorithm proposed. Specifically, Equation (26) serves as the critical mechanical decoder and enables the cross-dimensional demodulation of distributed tension vectors into environmental ice loading. Then, on this basis, Equation (27) further plays a boundary-anchoring role and establishes the regulatory threshold at which the biaxial tension ratio governs the consumption rate of the FEL. By deconstructing in-depth the physical compensation mechanism through which horizontal tension counteracts the vertical gravitational loading, this algorithm effectively corrects the inversion deviations induced by the FEL shielding effect during the early monitoring phase, which provides a more physically interpretable theoretical basis for load demodulation under extreme meteorological conditions. Subsequently, by replacing the total mass m in Equation (22) with the total mass m' of the iced fiber, the net cable mass m_0 with the net mass of the fiber span m_f, and the cable diameter d with the fiber diameter d_f, the relational expression linking the EIT to the designed FEL under icing conditions can be obtained and expressed as Equation (28).

$$i_f = \sqrt{\frac{z}{u_0 x} + \frac{{d_f}^2}{4}} - \frac{d_f}{2} \tag{28}$$

Furthermore, by combining Equation (20) with Equation (28) and rearranging the terms, the following relationship is obtained.

$$\eta_0 = \eta\left(i_f, \beta\right) = \frac{\beta a \sinh\left[\frac{\mu_0 x}{\beta a}\left({i_f}^2 + d_f i_f\right)\right]}{u_0 x\left({i_f}^2 + d_f i_f\right)} - 1 \tag{29}$$

Apparently, it establishes a nonlinear quantitative mapping relationship between the initial FEL η_0 and the equivalent ice load i_f of the bare optical fiber, and reveals that the i_f exhibits markedly differentiated evolutionary patterns across different stages of initial FEL depletion. The corresponding threshold for the i_f is relatively high when the optical fiber is in the high-redundancy stage. In contrast, as η_0 approaches ultimate critical zones of 0.7% and especially down to 0.1%, the response of the fiber on external equivalent loading undergoes an exponential transition and nonlinear amplification. In engineering, although the i_f retrieved via inversion from Equation (29) is physically distinct from the macroscopic meteorological ice accretion on the cable surface, this formulation enables graded and quantitative tracking of the optical fiber current stress severity based on biaxial micro-tensions and geometric characteristic parameters measured by BOTDR, once the internal FEL is depleted and the fiber transitions into the axially stressed stage.

All in all, a strong coupling relationship among FEL, instantaneous tension, and EIT is established here, which breaks away from the traditional limitation of treating the FEL parameter as static, transforms it into a dynamic characteristic that evolves with the icing state, and enables the real-time, refined inversion of FEL status based on tension metrics. Valuably, it compensates for the perception blind spot caused by the sudden change in mechanical response of the fiber optic stress state in traditional monitoring methods and provides a reliable micro-strain physical reference for the precise formulation of the differentiated anti-icing intervention decisions and the scientific setting of phased early warning thresholds under extreme ice loading conditions.

3. Experiments

Previous studies [32–34] conducted targeted experiments on optical fiber strength and attenuation in extremely harsh environments, yielding robust experimental datasets. We selected some representative segments of the same transmission optical cable line for experimentation, and chose OPGW power fiber optic cable as the research object, which includes standard traditional single-mode fiber G.652.D. All of the optical fibers adopted in the experiments were sourced from the same manufacturer, a uniform production batch, and a matching model series. To center the analysis on the core research objectives and ensure computational consistency, average values have been adopted for the material and geometric parameters of the G.652.D fibers, as shown in Table 1.

Table 1. Optical Fiber Characteristic Parameters.

Fiber Type	r (μm)	D_f (μm)	n_{co}	n_{cl}	V	Concent. (μm)
G652.D	4.2624	125.3734	1.468	1.459	2.101	0.0667

The focus of this article is to study the effect of icing on the strength of optical cables and the FEL of optical fibers, rather than the strength device of optical cables. Therefore, the classic strength testing setup [23,28] was used to conduct stress testing on the optical fiber within the iced cable segment, as shown in Figure 3. This is the typical simulation experimental platform for icing on overhead power transmission lines. Two adjustable

lifting brackets are each fitted with a fixed pulley, over which the optical fiber is routed to form a suspended span, whose terminal end is subsequently connected to the BOTDR monitoring system. Through this device, BOTDR can be used to demodulate and obtain the horizontal tension at the lowest point of the optical cable and the tension distribution data at the two end supports in real time. Simulated icing conditions can be reproduced by applying controlled loads to the optical fiber. Under ice loading, the actual arc length of the optical fiber within the span increases continuously, implying a corresponding variation in the equivalent FEL required to withstand external loads. As the critical parameter governing the operational lifespan of optical fiber, the properly configured excess length can provide effective mechanical buffering against external disturbances such as meteorological disasters.

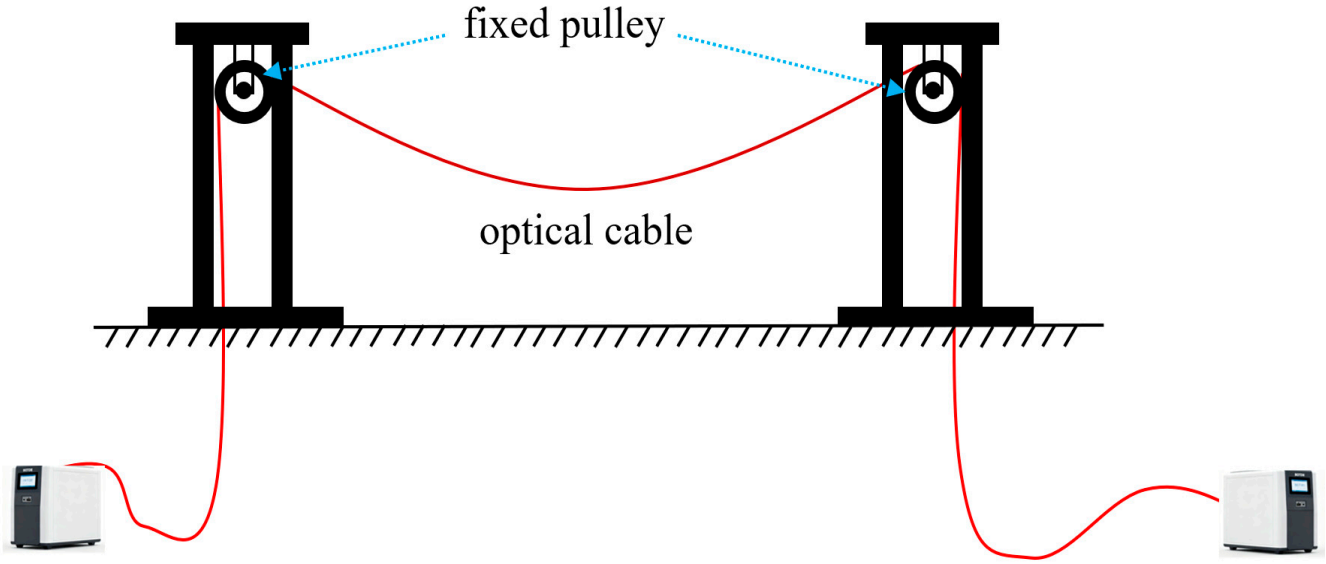

Figure 3. Schematic diagram of the simulation experiment device for icing on overhead power lines.

As is well known, the measurement cycle of fiber optic strength is very long, often lasting several months or even more [30,33,34]. However, conducting prolonged field experiments under extreme cold conditions to achieve this objective is impractical. Therefore, the strength testing platform was built in the laboratory, as shown in Figure 4a. Then, the on-site icing load under severe cold conditions was simulated by continuously adjusting environmental parameters. The strength of the optical fiber segments in stress can thus be tested, finally acquiring experimental results. For partial empirical outcomes, interested readers can refer to the on-site effect diagrams of stress–strain of optical cables listed by previous research [32], as shown in Figure 4b.

Specifically, in order to eliminate the influence of the fiber itself, ten samples were taken from each selected experimental object during the experiment, and it is assumed that the samples and their parameters in the same sample space are consistent. Furthermore, to ensure a more accurate comparative analysis of the experimental results, all subsequent tests were repeated for an identical number of experimental cycles. At the same time, to preclude potential interference arising from the instrumentation itself, this study assumes that all tools employed throughout the experimental process are clean, in optimal working condition, and used correctly.



(**a**)

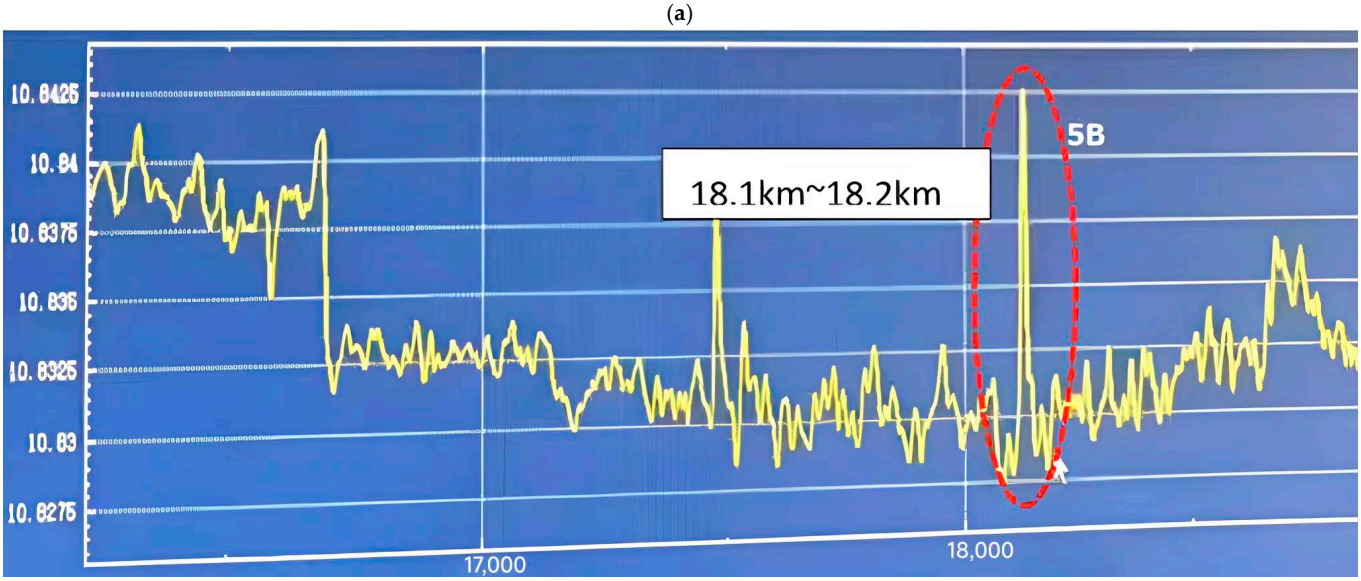

(**b**)

Figure 4. Physical photos (**a**). Physical image of optical cable stress–strain simulation experimental setup; (**b**) Enlarged curve diagram of local area around high stress point of the "5B" fiber obtained through BOTDR testing.

4. Discussion

Special attention must be paid to the conversion and unification of different units throughout all calculations and simulations presented.

4.1. The Relationship Between Tension and FEL

As mentioned previously, Equation (20) serves as the core analytical formula connecting macroscopic catenary geometry and the microscopic fiber strain state, quantitatively defining the control boundary of complex load field on the FEL consumption. This relationship manifests itself primarily on two levels. At first, it can directly yield two explicit quantitative boundaries. That the calculated FEL η approaches 0.1% signifies that the optical fiber is nearing a fully stretched state. At this moment, the system is poised to enter the high-sensitivity warning zone characterized by a sharp surge in strain. When η drops to 0%, it indicates that the initial excess length has been completely exhausted, and the optical fiber formally begins to bear axial strain, and consequently the safety boundary is substantively breached. These two thresholds partition the operational state into three distinct regimes, namely, Safe Zone ($\eta > 0.1\%$), Warning Zone ($0 < \eta \leq 0.1\%$), and Danger Zone ($\eta = 0$), which thus furnish the quantitative basis for implementing a multi-tiered early warning strategy. Secondly, the tension distribution varies with different positions of the optical fiber. Equation (20) maps spatial distribution of frequency shift to that of the FEL

consumption, thereby defining the local impact range of the icing load on the redundancy of optical fibers along the cable line. Thus, the game relationship between the horizontal tension and maximum tension of optical fiber in the dynamic evolution process of the FEL is precisely elucidated, whose simulation results are shown in Figure 5.

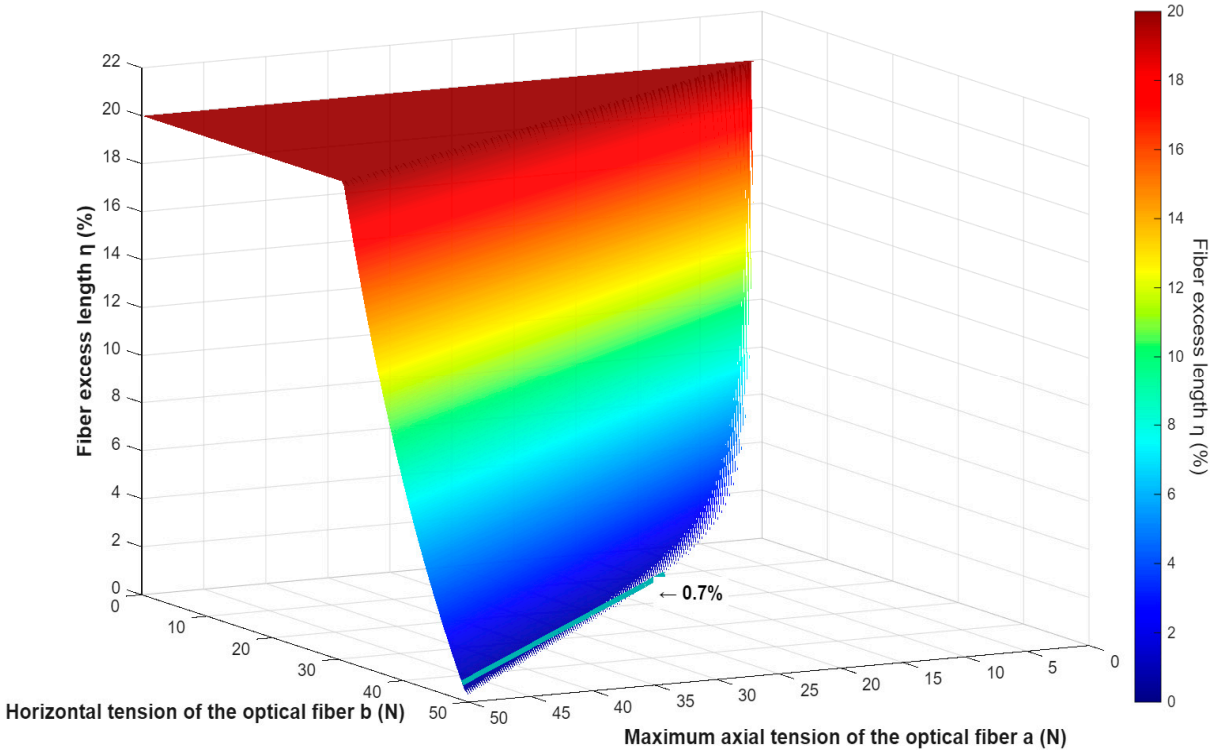

Figure 5. The game relationship between horizontal tension and maximum tension of optical fibers during the dynamic evolution of the FEL.

Over the micro-tension range of 0~50 N, Equation (20) imposes rigorous quantitative constraints on the nonlinear consumption boundary of the FEL under complex loading fields and establishes a direct mapping pathway between the biaxial micro-tensions, incorporating the maximum fiber tension a and the horizontal fiber tension b and the required initial FEL η_0, thus revealing the nonlinear evolution law of the optical fiber geometry rewinding process driven by biaxial tension coupling. Figure 5 further corroborates the evident negative physical correlation between the required initial FEL η_0 and the horizontal tension ratio $\beta = b/a$. As the value of β increases, the catenary sag of the optical cable is sharply compressed. The initial geometric redundancy η_0 required for system configuration shows an inverse proportional downward trend at this point, and it rapidly descends to the 0.7% critical boundary and even further into the 0.1% ultimate limit interval depicted in the figure.

Notably, this state of low design excess length under high β conditions does not signify enhanced mechanical safety margins. Rather, it reveals that the optical fiber has approached a vulnerable critical state wherein its geometric unwinding space is completely exhausted. When β asymptotically approaches 0.9955, the optical fiber is already in the critically straightened state under the self-weight of the cable. At this point, the system exhibits extremely high strain sensitivity to external environmental loads, requiring only 8.9 mm of initial ice accumulation to break this fragile mechanical equilibrium, and thus directly triggering a strain surge in the fiber optic body. This negative correlation furnishes explicit, differential design criteria for practical engineering applications. For transmission lines in heavy icing regions, β need to be actively reduced, and meanwhile accompanied

by a correspondingly larger initial FEL η_0 to provide sufficient geometric unwinding space against thick ice accretion. Conversely, for lines in light icing regions, β can be appropriately increased to permit smaller initial FEL and yet maintain the highly sensitive early-warning response to the incipient strain surges. This three-dimensional mapping model further reveals the boundary-anchored engineering optimization strategy by building upon the aforementioned critical-state evolution. By predicting the quantitative conclusion that the system can maintain zero strain criticality with only 0.1% design excess length under extreme tension conditions, namely β approaching 0.9955, engineering designers can adopt it as the safety baseline for anti-icing design. Further, for different expected ice thicknesses, the mapping relationship proposed can be used to reverse the initial FEL required for reasonable configuration, thereby avoiding the "one size fits all" redundant reservation in traditional design, and achieving precise and customized excess length configuration for specific ice conditions. This finding positions the horizontal tension ratio β as the pivotal mechanical adjustment lever that affects the differential configuration of initial FEL, providing theoretical support with both physical rigor and engineering operability for OPGW structure design and early warnings of ice damage under different ice conditions.

To further verify the physical reasonableness of Equation (20), published standard stress–strain test data for the typical OPGW specimens (RTS = 60 kN) under the IEEE 1138/IEC 60794-4/DL/T 832 [35–37] frameworks are referenced [32]. At an applied tension of 30 kN (50% RTS), the measured cable strain is approximately 0.62% and the corresponding fiber strain is approximately 0.28%. The initial FEL is thus back-calculated as $\eta_0 \approx 0.34\%$, which agrees well with the independently computed value of $\eta_0 \approx 0.32\%$ from Equation (20) using identical cable parameters, with a relative deviation of about 6%. Apparently, this result is also consistent with the typical design range of 0.5~0.7% reported in OPGW manufacturing standards, which confirms again that Equation (20) yields physically reasonable outputs under known cable structural parameters.

4.2. Coupling Analysis Between Tension and EIT

The inversion accuracy of ice cover thickness is improved by constraining the geometric shape of the catenary. Specifically, instead of relying solely on force data to directly calculate ice thickness, the geometric shape of the optical cable embodying arc length, inclination angle, and sag is included as the prior constraint in the inversion process to correct systematic errors introduced by traditional methods due to neglecting spatial shape changes. Equation (26) is employed to demodulate tension vectors acquired by the sensing terminal into environmental ice loading. By integrating it with Hooke's law, namely $F_c = A_c E_c \eta_0$, the three-dimensional physical state-space trajectory is constructed, which can elucidate the minimum required initial FEL η_0 necessary to ensure the optical fiber remains within its safe operating regime of zero axial strain across varying EIT i. Furthermore, the theoretical analysis has been conducted to visually demonstrate the evolutionary trend of equilibrium characteristics of the EIT under the biaxial tension dynamic evolution. The simulation results are shown in Figure 6.

In Figure 6, the vertical axis denotes the macroscopic cable tension F_c and the horizontal axes correspond to the required initial FEL η_0 and the EIT i, respectively. From the physical constraint characteristics of the evolutionary path, Hooke's law establishes a linear mapping between F_c and η_0. Equation (26) enables the quantitative correlation between the internal design parameter η_0 and the external environmental load i by introducing horizontal tension ratio β as a state variable. Furthermore, this state-space trajectory precisely delineates two critical boundaries for engineering design. For instance, the cyan circular marker in the figure denotes the design warning state, corresponding to $\beta = 0.9794$, $\eta_0 = 0.7\%$ and $i = 65.2$, which indicates that if the transmission line is exposed to the EIT

of approximately 65.2 mm, the initial FEL η_0 need to be designed to be at least 0.7% to ensure the OPGW remains free from axial fiber strain under this load. When more than 0.7% of the FEL designed is completely consumed by the external loads, the macroscopic cable tension F_c of the system reaches 115.7 kN, which can serve as the structural boundary for triggering the high-sensitivity warning. The ultimate critical point identified by the red circular marker in the figure, namely β = 0.9955, η_0 = 0.1%, and i = 8.9 mm, delineates the vitally important extremely early engineering boundary. Under the ultimate taut configuration of β = 0.9955 in the optical cable, the macroscopic cable tension F_c drops to the critical equilibrium state dominated by the self-weight of the optical cable, at which F_c = 24.9 kN. It is worth noting that an EIT of only 8.9 mm is required to completely exhaust the geometric rewinding space inside optical fiber under this extreme tension condition, which is equivalent to providing the clear lower limit criterion for the design. For example, for operating conditions with an ice cover thickness of 8.9 mm, the initial FEL η_0 of OPGW design only needs to be strictly greater than 0.1%, namely $\eta_0 > 0.1\%$, to ensure that the optical fiber remains within the safe zone under this load without axial tensile strain. In summary, the high degree of self-consistency between Hooke's law and Equation (26) within the framework of cross-scale mechanical analysis is substantiated in Figure 6. Here, we also translate explicitly the abstract micro-strain metric into the quantitative design thresholds tailored to the specific icing regions. That is, to cope with ice cover levels of 65.2 mm and 8.9 mm, the initial FEL design values η_0 of optical fiber must be greater than 0.7% and 0.1%, respectively. It provides a strict theoretical basis for the differentiated process design, early warning threshold setting for icing, and line safety redundancy configuration of the OPGW optical cables under the extreme weather conditions.

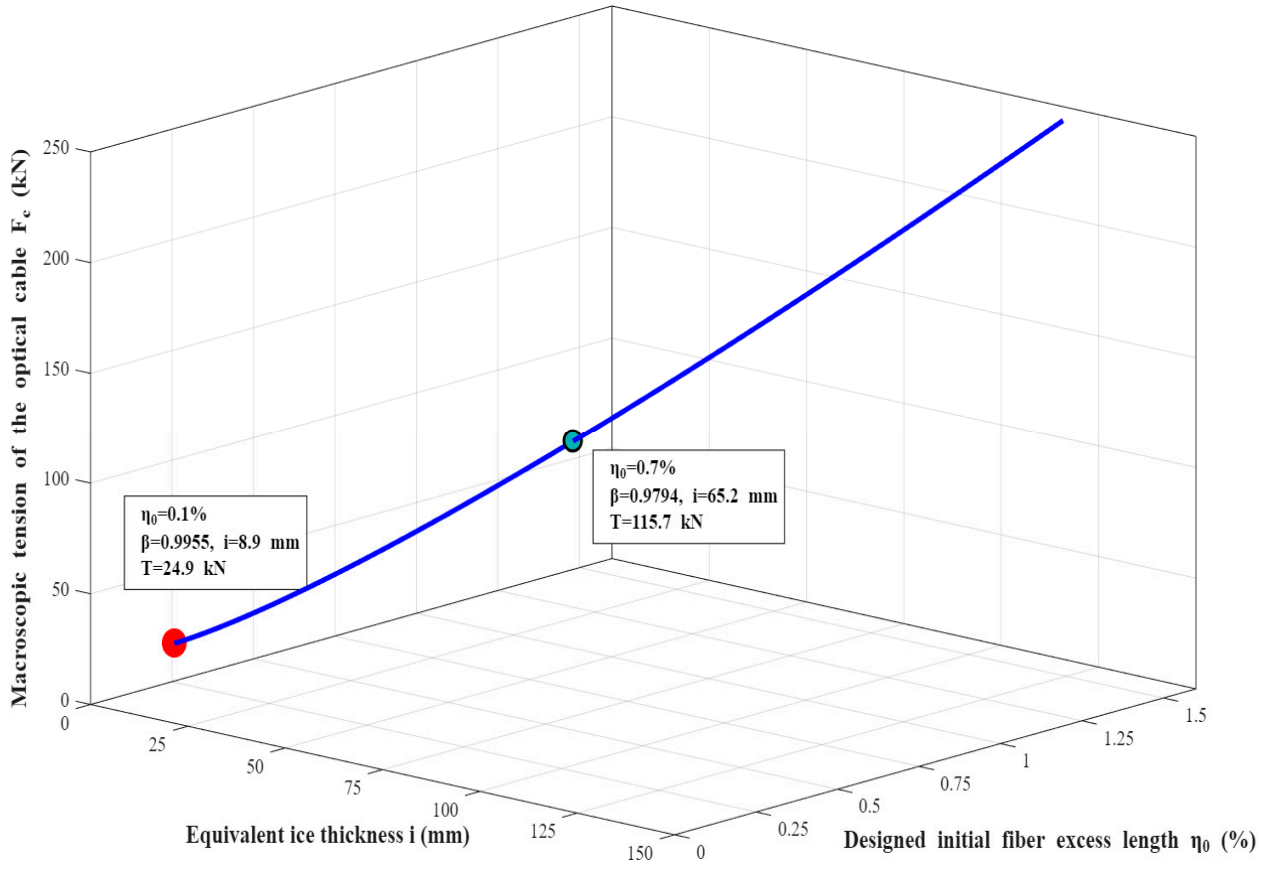

Figure 6. Equilibrium characteristics of equivalent ice thickness under biaxial tension dynamic evolution.

To further validate the availability of the Equation (26), the classical catenary state equation, widely used for ice-overloaded OPGW assessment, is adopted as a numerical benchmark. For a 300 m span with $EA = 1.65 \times 10^7$ N and $q_0 = 9.8$ N/m, the macroscopic tension F_c is computed over an ice thickness range of 0–80 mm using both the classical state equation and Equation (26). The maximum relative deviation between the two datasets is 4.7%, and it decreases as ice thickness increases. In addition, according to the IEC 60794-4 [36] specification for the "no fiber strain condition" (fiber strain $\leq 0.05\%$ at 85% RTS), the proposed model predicts that $\eta_0 > 0.6\%$ is required for the benchmark parameters, which is fully consistent with the standard, proving again that Equation (26) is physically consistent with the established OPGW mechanical models.

4.3. The Relationship Between EIT and FEL

Although Equation (27) establishes the nonlinear mapping relationship among the optical FEL η, EIT i, and biaxial tensions, namely maximum tension F_x and horizontal tension F_H, the single tension dimension cannot independently characterize the coupling behavior among these three parameters. Specifically, although Equations (20) and (26) establish the pairwise mapping relationships between tension and FEL and tension and EIT, both rely on the maximum tension F_x as the implicit intermediate parameter and neither can intuitively capture the direct correspondence between icing severity and the internal state of the optical fiber. Further, the horizontal tension ratio $\beta = F_H/F_x (0 \leq \beta < 1)$ is introduced as the third independent variable, which is equal to the cosine value of inclination angle θ of the suspension point in catenary geometry, i.e., $\beta = cos\theta$, and can intuitively describe the steepness of the catenary. Evidently, the introduction of the β extends Equation (27) from the two-dimensional mapping to the three-dimensional spatial mapping. For instance, when β is held constant, the model yields an explicit functional relationship wherein the given EIT i maps directly to the unique FEL η. That is, each group (i,β) uniquely corresponds to the η, thus achieving the one-to-one mapping of that from ice load input to excess length output.

However, when the initial FEL is fully exhausted by extreme ice loading and the system transitions into the operational regime where the bare optical fiber directly bears axial stress, the mapping relationship established by Equation (27) between macro-scale ice thickness and the designed FEL no longer suffices to quantify the risk of the sharp surges in the subsequent micro-strain within optical fiber itself. Equation (29) constructs a high-sensitivity inversion model for the ultimate axial load-bearing regime using the micron-scale characteristic diameter d_f of the bare optical fiber and dynamically analyzes the geometric characteristic term z of the catenary as experimentally measured by BOTDR and the biaxial micro-tension ratio β, eventually mapping the magnitude of axial stress sustained by the optical fiber onto the equivalent ice load i_f imposed on the bare optical fiber. Although the i_f is physically distinct from the macroscopic meteorological ice accretion on the optical cable sheath, its incorporation establishes the rigorous functional closed loop integrating the FEL configuration capability of Equation (27) during the design phase with the axial load tracking capability of Equation (29) in the ultimate load-bearing regime. In other words, the former serves to establish passive safety design thresholds whereas the latter enables dynamic tracking of axial stress and graded hazard classification following the complete depletion of the FEL. Additionally, these two equations have been jointly analyzed to achieve cross physical scale coverage from passive safety design to ultimate micro-strain monitoring, which provides the comprehensive theoretical foundation for both full-life-cycle mechanical assessment of in-service OPGW cables and the formulation of differentiated anti-icing strategies under extreme ice loading conditions.

Immediately thereafter, the three-dimensional nonlinear mapping relationship among the biaxial tension ratio, equivalent ice loading, and initial FEL is established using Equations (27) and (29), which is then transformed into two complementary three-dimensional evolution diagrams through systematic theoretical analysis and numerical simulation, as shown in Figures 7 and 8. Among them, Figure 7 is dedicated to quantifying design-oriented safety margins and establishing criteria for differentiated icing-zone configuration, while Figure 8 focuses on dynamic tracking of mechanical responses in the ultimate axial load-bearing regime following the complete depletion of the initial FEL. The two together constitute the full-life-cycle quantitative evaluation basis for the mechanical stress of OPGW cables, spanning from the engineering design to the ultimate micro-strain monitoring.

Figure 7 visually illustrates the minimum initial fiber redundancy configuration required to ensure that the fiber body does not generate axial strain throughout its service life under different tensile tautness and external ice load conditions. Furthermore, the distribution of the required initial FEL η_0 presents the pronounced, inherently nonlinear characteristic jointly governed by the horizontal tension ratio β and the EIT i, which can be partitioned into three representative physical regimes according to the underlying stress–strain protection mechanism, and are then as follows.

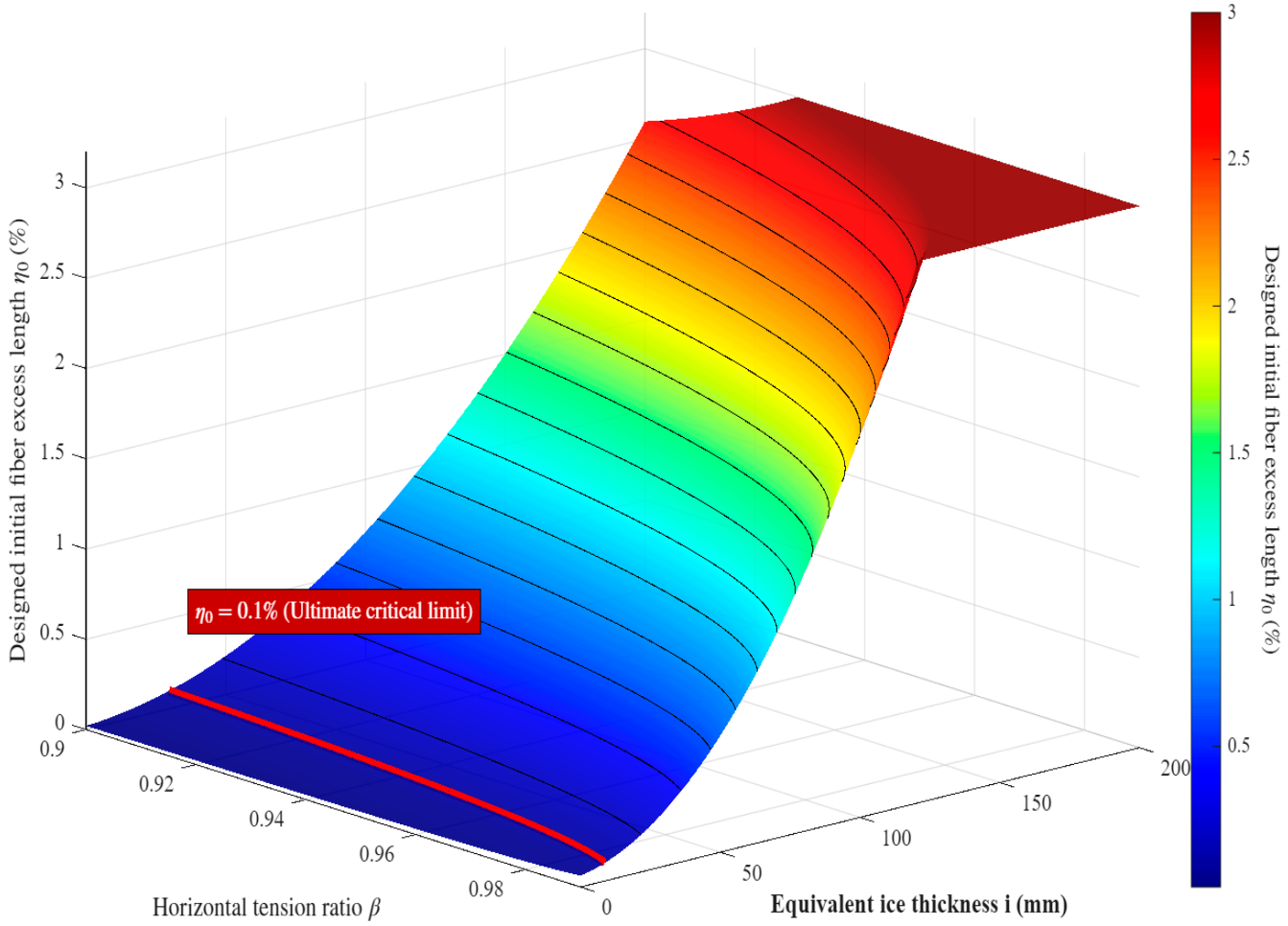

Figure 7. Relationship between design safety margin and differentiated ice area configuration.

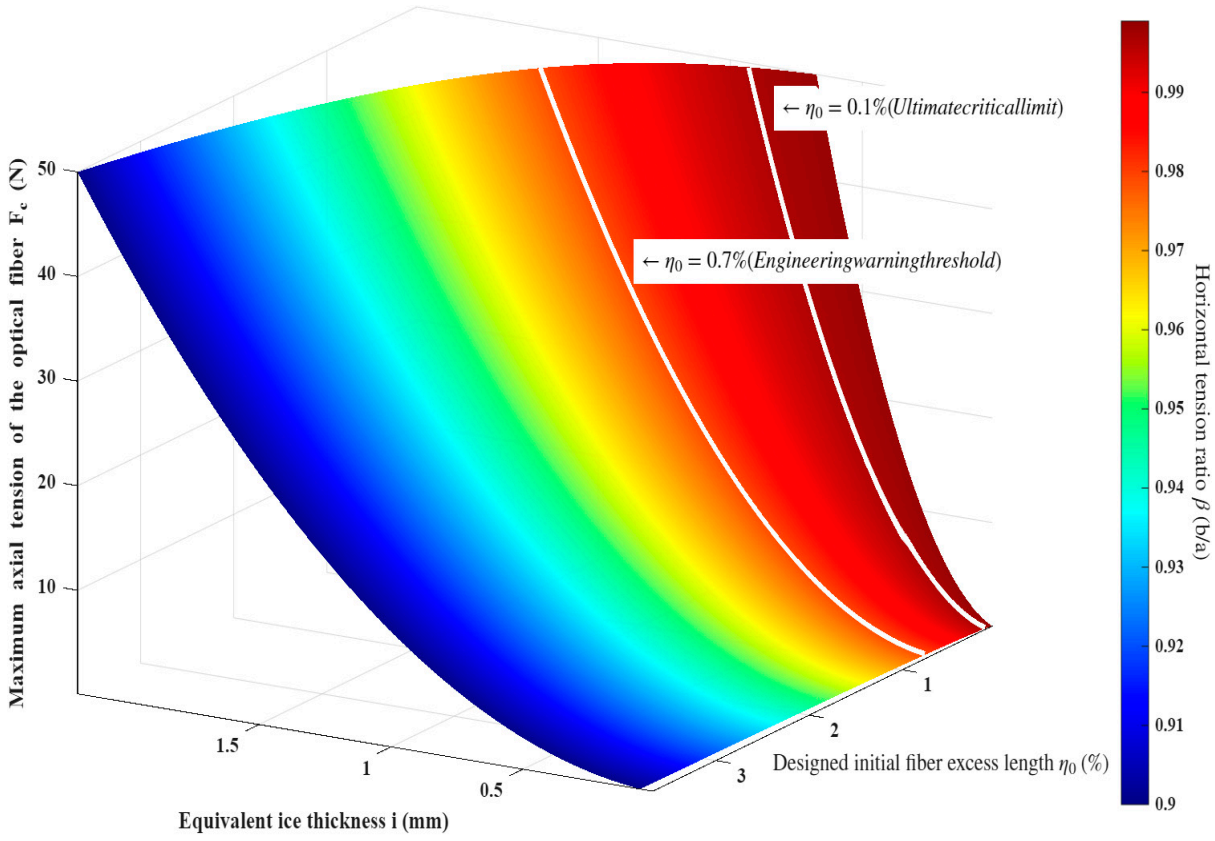

Figure 8. Relationship between ultimate micro-strain load-bearing regime and ice accretion evolution.

(1) High Excess Length Safety Zone (η_0 > 1.0%). Within the range of defined typical OPGW engineering parameters, the three-dimensional mapping surface exhibits the prominent, elevated red flat-top area when the horizontal tension ratio β < 0.92 and the cable is under light ice loading. The required threshold for the initial FEL η_0 is comparatively lenient under this condition. However, due to the large sag of the catenary, the elongation of the cable caused by external ice load can be effectively absorbed by the wavy geometric rewinding inside optical fiber, such that the fiber body is in a completely relaxed state and the BFS signal resides in the geometric shielding range. It is worth noting that this geometric rewinding process is based on the premise that the fiber optic cable shell structure is in the elastic deformation stage. Besides, the axial stiffness term A_cE_c of the fiber optic cable structure serves as the denominator term in Equation (27), essentially constituting the elastic constraint boundary for the transmission of macroscopic deformation to microscopic geometric rewinding.

(2) FEL Intense Consumption and Coupling Evolution Zone (0.1% < η_0< 1.0%). When the EIT i increases continuously or the horizontal tension ratio β approaches 0.98, the three-dimensional mapping surface plunges rapidly from the red plateau to the yellowish-green transition zone. At this point, the physical response exhibits pronounced nonlinearity that for a fixed EIT i. Even a marginal increment in the horizontal tension ratio β can lead to a sharp surge in the required initial FEL η_0. Furthermore, this area reveals a critical design principle, that is, under the same icing level, the smaller the catenary sag of optical cable during installation, i.e., the larger β, the more stringent the initial FEL η_0 requirement that the system must equip to ensure fiber safety becomes, and the more obvious the shift of critical point for the transition from geometric rewinding to elastic deformation in the system becomes.

(3) Deep Early-Warning Transition Zone (0.2%$\leq\eta_0 \leq$ 0.5%). Within this interval, the descent gradient of the three-dimensional surface enters a regime of precipitous amplification, and thus the engineering safety margin is drastically compressed. When the required initial FEL η_0 drops to 0.5%, the widely recognized lower structural safety limit in the OPGW engineering sector, the system has substantively lost its conventional ice-resistant redundancy, marking the entry of the optical cable body into the highly sensitive stress pre-control zone under external disturbances. Should conditions deteriorate further to the initial FEL η_0 = 0.2, the geometric unwinding space within the optical fiber is on the verge of the full exhaustion, such that minor environmental fluctuations are directly converted into localized stress concentrations in the fiber itself. The BOTDR monitoring signal within this deep early-warning section can no longer be regarded as the stable background noise, but should be used as the precursor trigger signal for imminent structural damage caused by ice disasters.

(4) Axial Strain Critical Early-Warning Zone ($\eta_0 \leq$ 0.1%). The surface at the bottom of the graph that is jointly demarcated by the dark blue area and the bold red solid line constitutes the absolute ultimate critical safety baseline of η_0 = 0.1%. When the system operational state approaches this critical threshold plane, regardless of the combination of external ice thickness and cable tension configuration, the initial FEL inside the optical fiber has been compressed to the limit edge. In addition, the optical fiber has essentially exhausted its geometric unwinding capacity and transitions into a hazardous state of full axial load bearing when the system operates below this critical plane. Under these conditions, any marginal increment in external loading or minor perturbation to the tensioning regime can directly induce a sharp surge in axial strain within the fiber itself. Meaningfully, the bold red critical baseline corresponding to η_0 = 0.1% not only serves as the lower safety bound for OPGW engineering design, but also constitutes ultimate criterion for triggering structural fracture early warnings in the ice monitoring model proposed under extreme operating conditions.

In a word, when the EIT i falls within the light loading regime of 0~50 mm, the three-dimensional mapping surface resides in a low-altitude blue-green region, and thus the required initial FEL η_0 generally remains at a low magnitude of 0.2~0.8%. As the i increases to the 50~100 mm range, the surface rises into the yellowish-green transition zone and the required η_0 surges to 1.0~1.8%. When the EIT i further rises to 100~150 mm or even 150~200 mm, the surface enters the steep red elevated zone, and at this point the required η_0 escalates to 1.8~3.0% or even higher. The climbing rate shows a significant acceleration trend when the horizontal tension ratio β approaches 0.98. Significantly, the pivotal role of β as the core mechanical leverage point is further corroborated. Mathematically, the term $\sqrt{1-\beta^2}$ in the denominator of Equation (27) undergoes precipitous convergence to zero as the β approaches 0.99, thus causing minor geometric deformations induced by equivalent ice accretion to be nonlinearly amplified through this mathematical structure, which is exactly the fundamental dynamic reason why the system is extremely sensitive to small changes in the ice thickness. Further, the smaller the β, the larger the mechanical tolerance margin of the system against vertical ice loading becomes, and the lower the required initial FEL η_0 becomes. The more closely β approaches 1.0, the earlier the system enters its critical mechanical boundary. The quantitative conclusion, derived from the analysis of specific EIT intervals, provides strict and operable theoretical support for differentiated manufacturing process design of in-service OPGW optical cables, dynamic setting of distributed micro-strain early-warning thresholds, and the formulation of anti-icing disaster strategies in severe cold regions.

In Figure 8, the differential evolution law between the EIT i_f and macroscopic tension a at different initial FEL η_0 is accurately revealed. The vertical axis denotes the macroscopic

tension F_x (0~50 N) experienced by the optical fiber during actual mechanical loading. The horizontal biaxial represents the direct load i_f (0~2 mm) caused by the equivalent ice layer of the bare optical fiber and the geometric rewinding redundancy η_0 (0~4%) reserved inside the optical fiber, respectively. The continuous evolution of the surface color gradient intuitively maps the distribution characteristics of the horizontal tension ratio $\beta = b/a$ between 0.90 and 0.999. The two prominent white physical boundary lines in the figure anchor the engineering early-warning threshold at $\eta_0 = 0.7\%$ and the limit critical line at $\eta_0 = 0.1\%$, respectively.

When the initial FEL η_0 resides within the high-redundancy range of 3.0~4.0%, the system retains ample geometric unwinding buffer capacity, and the three-dimensional mapping surface manifests as the low-lying blue region. This moment, the fiber exhibits an exceptionally large mechanical tolerance margin against the EIT i_f, while the required macroscopic maximum tension F_x remains anchored at a low baseline level. As the initial FEL η_0 approaches 0% or the i_f on the bare optical fiber increases, the slope of the three-dimensional surface undergoes the precipitous rise and rapidly transitions into the steep, elevated dark red zone. Especially under extreme tension conditions where the horizontal tension ratio β approaches 0.99 or above, the steep slope feature in the upper right corner of the graph is particularly prominent, and a very small increment of i_f can induce the sharp increase in the maximum tension F_x of the optical fiber, indicating that once the geometric unwinding space within the optical fiber is drastically compressed, the strain response of the system to external equivalent loads exhibits exponential transitions and nonlinear amplification. Notably, the EIT i_f of bare optical fiber derived from inverting Equation (29) is physically distinct from the macroscopic ice accretion on the optical cable's surface. But after the internal FEL is fully exhausted and transferred to the bare fiber body to directly bear external loads, this equation can be based on the geometric characteristic terms measured by BOTDR and the proportion of biaxial micro-tension β, to continuously classify and quantify the current actual stress severity of optical fiber, and then rectify physical sensing blind zones inherent to conventional monitoring techniques during phases of abrupt fiber mechanical response transitions. In addition, the bottom limit critical line in the picture, namely $\eta_0 = 0.1\%$, is the watershed of this force stage, indicating that the geometric rewinding redundancy inside the optical fiber has completely returned to zero, which means that the system has officially entered the critical equilibrium state dominated by self-gravity and extremely thin ice layers. In particular, the lower the β, the greater the mechanical tolerance space of the system to icing loads becomes, while the higher the β, the more exponentially amplified strain sensitivity of the system to changes in the external ultra-thin ice layer.

Comparing Figures 7 and 8, it can be seen that the former focuses on the initial FEL configuration under the differentiated ice zones based on Equation (27) and positions the β as the core mechanical control lever, which specifies the initial FEL required for the system under different EIT levels (0~200 mm), and provides a pre-quantitative benchmark for differentiated process design and safety margin assessment of OPGW optical cables. Figure 8 centers on the axial load-bearing stage after the FEL is exhausted based on Equation (29) and adopts the EIT i_f of the bare fiber as the high-sensitivity reference index to achieve continuous grading and quantification of the severity of the fiber stress. Obviously, the combination of the two not only constructs the complete theoretical chain from passive safety design to extreme force monitoring, but also provides theoretical support for OPGW power cable operation and maintenance decisions under extreme ice disaster conditions.

5. Conclusions

This study makes the following main contributions to the monitoring of in-service OPGW power optical cables under icing conditions. (1) The BOTDR-based distributed stress–strain field acquisition method has been established and a catenary–biaxial static coupling model has been proposed to correlate the macroscopic mechanical responses, including maximum tension and horizontal tension, with two key microscopic state parameters, namely FEL and EIT. (2) The coupled intervention mechanism connecting EIT, distributed tension, and FEL has been revealed, showing that the inhibitory effect of horizontal tension on FEL is significantly enhanced with increasing icing load. (3) The quantitative evaluation method for the remaining percentage of FEL in OPGW power cables has been proposed by monitoring the BFS offset. (4) The derived inversion formulations are cross-validated against the classical catenary state equation and published OPGW stress–strain test data, with deviations within 6%, confirming their physical reasonableness under the known cable structural parameters. (5) The proposed model provides the theoretical basis for the structural design, hazard investigation, and ice disaster early warning of OPGW optical cables.

Author Contributions: Conceptualization, L.H. and C.L.; methodology, L.H.; software, Y.L.; validation, L.H., C.L. and Y.L.; formal analysis, Y.L.; investigation, Y.L.; resources, C.L.; data curation, C.L.; writing—original draft preparation, Y.L.; writing—review and editing, L.H. and Y.L.; visualization, Y.L.; supervision, C.L.; project administration, L.H.; funding acquisition, C.L. All authors have read and agreed to the published version of the manuscript.

Funding: This work is supported by Science and Technology Project of State Grid Corporation of China (SGHNTX00SYJS2400186) and Research project of Guangdong TeFa Information Optical Cable Co., Ltd. (2025ZKHX401).

Data Availability Statement: No new data were created or analyzed in this study. Data sharing is not applicable to this article.

Acknowledgments: The authors would like to thank the editor and the reviewers for their reviews and suggestions to help us improve the quality of this paper.

Conflicts of Interest: We declare that we have no financial and personal relationships with other people or organizations that can inappropriately influence our work reported in this manuscript, and there is no professional or other personal interest of any nature or kind in any product, service and/or company that could be construed as influencing the content presented in, or the review of, the manuscript entitled.

References

1. Binh, L.N. *Optical Fiber Communication Systems with MATLAB and Simulink Models*; CRC Press: Boca Raton, FL, USA, 2014.
2. Neumann, E.G. *Single-Mode Fibers: Fundamentals*; Springer: Berlin/Heidelberg, Germany, 1988; Volume 57.
3. Burdin, V.A.; Vazhdaev, M.A. Method of excess fiber length estimating based on low subzero temperature climatic test. *Int. Soc. Opt. Photonics* **2014**, *vol.9156*. [CrossRef]
4. Andreev, V.A.; Gavryushin, S.A.; Popov, B.V.; Popov, V.B.; Vazhdaev, M.A. Statistical characteristics of excess fiber length in loose tubes of optical cable. In Proceedings of the XIV International Scientific and Technical Conference on Optical Technologies in Telecommunications, Samara, Russia, 6 April 2017.
5. Cui, Z.; Yuan, C.; Xu, K.; Sun, Y.; Yin, S. Modeling the splice loss of ultra-low loss fiber and single-mode optical fiber in high altitude area. *Opt. Fiber Technol.* **2021**, *67*, 102696. [CrossRef]
6. Hu, L.; Yuan, C. Analysis of Splice Loss of Single-Mode Optical Fiber in the High Altitude Environment. *Coatings* **2021**, *11*, 876. [CrossRef]
7. Alekchin, I.N.; Burdin, V.A. Prony decomposition algorithm for processing polarization reflectometry data to determine the distributions of excess optical fiber length in a cable. In Proceedings of the SPIE Conference on Optical Technologies for Telecommunications, Kazan, Russian, 22 May 2020.

8. Burdin, V.A. The method for a measurement of the excess fiber length on the cable delivery length by using the polarization reflectometry. In Proceedings of the XIV International Scientific and Technical Conference on Optical Technologies in Telecommunications, Samara, Russian, 22–24 November 2016; Volume 10342, p. 9.
9. Bin, F.; He, J.; Qiu, K.; Hu, L.; Zheng, Z.; Sun, Q. CI-YOLO: A lightweight foreign object detection model for inspecting transmission line. *Measurement* **2025**, *242*, 116193. [CrossRef]
10. Ghatak, A.; Thyagarajan, K. *Introduction to Fiber Optics*; Cambridge University Press, Information and Communication Engineers: Cambridge, UK, 1998.
11. Brown, D.C.; Hoffman, H.J. Thermal, stress, and thermo-optic effects in high average power double-clad silica fiber lasers. *IEEE J. Quantum Electron.* **2001**, *37*, 207–217. [CrossRef]
12. Xu, K.H.; Yuan, C. A Fault Location Analysis of Optical Fiber Communication Links in High Altitude Areas. *Electronics* **2023**, *12*, 3728. [CrossRef]
13. Poddubrovskii, N.R.; Kovalenko, D.A.; Lobach, I.A.; Kablkov, S.I. 50-km distributed strain sensing enabled by a self-swept BOTDR. *Opt. Commun.* **2026**, *620*, 133561. [CrossRef]
14. Huang, H.; Lv, Q.; Mao, D.; Hao, Y.; Zeng, H.; Wu, Y. A Method Employing Micrometeorological Data to Decouple BOTDR Monitoring of Temperature and Stress for the Measurement of Ice Thickness on Optical Fiber Composite Overhead Ground Wire. In Proceedings of the 8th International Conference on Advanced Algorithms and Control Engineering (ICAACE), Shanghai, China, 9 June 2025.
15. Gao, K.; Li, J.; Wang, Y.; Zeng, S.; Li, B.; Rao, Y. Frequency-and-Time Division Multiplexed Brillouin Optical Time-Domain Reflectometry. *Photonic Sens.* **2026**, *16*, 9560005. [CrossRef]
16. Wang, H.P.; Guo, C.Y.; Wei, D.Y.; Wang, X.Z.; Xiang, P.; Dai, J.G.; Ni, Y.Q.; Ou, J.P. Optical fiber sensing information driven structural feature parameter reflection, damage identification and state assessment: A review. *Chin. J. Appl. Mech.* **2026**, *43*, 748–766.
17. Gong, Z.; Yan, C.-L.; Ma, J.; Yi, D.-F.; Cao, P.-F.; Wang, H.-P. Real-time vacuum degree characterization of aerospace vacuum pressure vessels based on FBG monitoring information. *Meas. Sci. Technol.* **2026**, *37*, 015102. [CrossRef]
18. Girard, S.; Morana, A.; Ladaci, A.; Robin, T.; Mescia, L.; Bonnefois, J.-J.; Boutillier, M.; Mekki, J.; Paveau, A.; Cadier, B.; et al. Recent advances in radiation hardened fiber-based technologies for space applications. *J. Opt.* **2018**, *20*, 093001. [CrossRef]
19. Xia, M.; Tang, X.H.; Wang, Y.; Li, C.; Wei, Y.; Zhang, J.; Jiang, T.; Dong, Y. OPGW positioning and early warning method based on a Brillouin distributed optical fiber sensor and machine learning. *Appl. Opt.* **2023**, *62*, 1557–1566. [CrossRef] [PubMed]
20. Bao, X.; Zhou, D.P.; Baker, C.; Chen, L. Recent Development in the Distributed Fiber Optic Acoustic and Ultrasonic Detection. *J. Light. Technol.* **2017**, *35*, 3256–3267. [CrossRef]
21. Yablon, A.D. *Optical Fiber Fusion Splicing*; Springer: Berlin/Heidelberg, Germany, 2005.
22. Bogachkov, I.V.; Trukhina, A.I.; Gorlov, N.I. Detection of Optical Fiber Segments with Mechanical Stress in Optical Cables Using Brillouin Reflectometers. In Proceedings of the International Siberian Conference on Control and Communications (SIBCON), Tomsk, Russia, 6 June 2019.
23. Shang, H.; Huang, Z. OPGW cable icing status monitoring based on BOTDR. *AIP Conf. Proc.* **2019**, *2073*, 020065. [CrossRef]
24. Guo, M.; Hao, Y.; Zheng, Y.; Chen, B.; Yu, X.; Li, L. BOTDR Monitoring of Tensile State in Three-Core Fiber-Optic Composite Submarine Cables with a Three-Layer Mechanical Structure and Dual-Threshold Sensing Model. *J. Mar. Sci. Eng.* **2026**, *14*, 390. [CrossRef]
25. Zhang, Z.; Zhang, H.; Yue, S.; Zeng, W. A Review of Icing and Anti-Icing Technology for Transmission Lines. *Energies* **2023**, *16*, 601. [CrossRef]
26. Tan, M.; Zhou, N.; Wang, J.; Zou, D.; Zhang, W.; Mei, G. A real-time impact detection and diagnosis system of catenary using measured strains by fibre Bragg grating sensors. *Int. J. Veh. Mech. Mobil. Veh. Syst. Dyn.* **2019**, *57*, 1924–1946. [CrossRef]
27. Huang, W.; He, D.; Tong, D.; Chen, Y.; Huang, X.; Qin, L.; Fei, Q. Static analysis of elastic cable structures under mechanical load using discrete catenary theory. *Fundam. Res.* **2023**, *3*, 967–973. [CrossRef] [PubMed]
28. Suchocki, C.; Rutkiewicz, A.; Katzer, J.; Kowalska, E. Remote estimation of cable tension using catenary theory and point clouds obtained by terrestrial laser scanning. *Measurement* **2024**, *236*, 115147. [CrossRef]
29. Dou, Z.; Wang, Y.; Cong, L.; Huang, W.; Zhang, Q.; Hu, Y.; Bi, Y. Study on the Wind-Induced Vibration Response of OPGW Cables under Icing Conditions. In Proceedings of the International Conference on Electronic Information Engineering and Computer (EIECT), Shenzhen, China, 13 February 2025.
30. Griffioen, W.W. Optical Fiber Mechanical Reliability. Doctoral Dissertation, Eindhoven University of Technology, Eindhoven, The Netherlands, 1995.
31. Turatbek, B.D.; Dikarev, D. Implementation of Some Non-Classical Mathematical Models of the Mechanics of a Deformable Body in the MathCad and MatLab System. In Proceedings of the International Conference on Information Technologies in Engineering Education (Inforino), Moscow, Russia, 12–15 April 2022.

32. Zhang, G.; Wang, D.; Li, J.; Li, C.; Miao, H.; Hu, L. Practice and importance analysis of strain measurement in optical cable operation and maintenance. *Wire Cable* **2025**, *68*, 29–35.
33. Hu, L.W.; Yuan, C.W. Modeling and analysis of the fusion strength of single-mode optical fiber in the high altitude environment. *Opt. Mater. Express* **2022**, *12*, 2995–3014. [CrossRef]
34. Hu, L.W.; Yuan, C.W. Improvement in fusion performance between G652.D fiber and Ultra-low-loss fiber by controlling discharge current of fusion splicer. *Opt. Fiber Technol.* **2023**, *79*, 103368.
35. *IEEE 1138-2021*; IEEE Standard for Testing and Performance of Optical Ground Wire (OPGW) for use on Electric Utility Power Lines. IEEE: Piscataway, NJ, USA, 2021.
36. *IEC 60794-4:2018*; Optical Fibre Cables—Part 4: Sectional Specification-Aerial Optical Cables Along Electrical Power Lines. IEC: Geneva, Switzerland, 2018.
37. *DL/T 832-2016*; Optical Fiber Composite Overhead Ground Wires. National Energy Administration: Beijing, China, 2016.

Disclaimer/Publisher's Note: The statements, opinions and data contained in all publications are solely those of the individual author(s) and contributor(s) and not of MDPI and/or the editor(s). MDPI and/or the editor(s) disclaim responsibility for any injury to people or property resulting from any ideas, methods, instructions or products referred to in the content.